ANNUAL REVIEWS

Annual Review of Condensed Matter Physics

Fractional Quantum Anomalous Hall Effect

Ting Cao,[1] Liang Fu,[2] Long Ju,[2] Di Xiao,[1,3] and Xiaodong Xu[1,3]

[1]Department of Materials Science and Engineering, University of Washington, Seattle, Washington, USA; email: tingcao@uw.edu, dixiao@uw.edu, xuxd@uw.edu

[2]Department of Physics, Massachusetts Institute of Technology, Cambridge, Massachusetts, USA; email: liangfu@mit.edu, longju@mit.edu

[3]Department of Physics, University of Washington, Seattle, Washington, USA

Annu. Rev. Condens. Matter Phys. 2026. 17:233–56

First published as a Review in Advance on December 22, 2025

The *Annual Review of Condensed Matter Physics* is online at conmatphys.annualreviews.org

https://doi.org/10.1146/annurev-conmatphys-031524-071133

Keywords

quantum Hall effect, zero magnetic field, topology, twisted $MoTe_2$ bilayer, rhombohedral-stacked multilayer graphene

Abstract

The realization of the fractional quantum anomalous Hall effect (FQAHE) in a zero-field fractional Chern insulator is a new advancement in condensed matter physics, resulting from the interplay among strong correlations, topology, and spontaneous time-reversal symmetry breaking in lattice systems. In this review, we highlight the experimental and theoretical progress toward achieving FQAHE in two material platforms: twisted bilayer $MoTe_2$ and rhombohedral-stacked multilayer graphene. These systems host narrow topological bands with nontrivial Chern numbers, enabling interaction-driven fractionalized states analogous to the fractional quantum Hall effect, but without external magnetic fields. We discuss how spontaneous ferromagnetism, moiré lattice reconstruction, and band topological effects underpin the emergence of FQAHE in twisted $MoTe_2$. We describe experimental discoveries of zero-field fractional Chern insulators in both transport and optical experiments, as well as signatures of composite Fermi liquids and higher-energy Chern band, which may shed light on engineering nonabelian states. In rhombohedral graphene/hexagonal boron nitride moiré superlattices, we review the recent observations of fractionally quantized Hall resistance, connections between FQAHE and extended quantum anomalous Hall phases, and the coexistence of

superconductivity and FQAHE. These discoveries not only deepen our understanding of strongly correlated topological matter but also open new frontiers for exploring nonabelian anyons, fault-tolerant quantum computation, and topological opto-spintronics free of magnetic fields.

1. INTRODUCTION

A vibrant frontier in modern condensed matter physics is the study of topological quantum many-body systems, in which the interplay between topology and electron–electron interactions gives rise to exotic quantum phases of matter. A seminal example is the integer quantum Hall effect (IQHE) discovered in 1980 (1). In a two-dimensional (2D) electron gas subjected to a strong perpendicular magnetic field, the formation of Landau levels leads to a remarkable quantization of the Hall resistance (R_{xy}) in integer multiples of $\frac{h}{e^2}$, accompanied by a vanishing longitudinal resistance (R_{xx}). Two years later, similar quantization of R_{xy} and suppression of R_{xx} were observed at fractional fillings ($\nu = \frac{1}{3}$) of the lowest Landau level (LLL) in high-mobility GaAs samples (2). This phenomenon, known as the fractional quantum Hall effect (FQHE), arises from electron–electron interactions in partially filled Landau levels and represents a class of electronic phases that lie beyond the conventional Landau symmetry-breaking paradigm (3). Instead, these phases are characterized by the emergence of fractional quasiparticle and topological order. Beyond their fundamental importance, insights from the FQHE and related systems have profoundly influenced the development of fault-tolerant topological quantum computation, leveraging features such as anyonic excitations with nonabelian statistics (4–18). The quantized Hall conductance in both the IQHE and the FQHE has been identified as a topological invariant known as the Chern number (19, 20), which now underpins the characterization of Chern insulators. Notably, the Chern number of the many-body ground states is universally defined for all gapped quantum states in two dimensions, and a nonzero Chern number does not require the presence of a magnetic field (20), suggesting that both the IQHE and the FQHE may be realized in systems without an external magnetic field.

The idea of realizing the IQHE without Landau levels has been extensively explored and experimentally achieved. A groundbreaking step was Haldane's proposal of a model on the honeycomb lattice that exhibits the IQHE in the absence of an external magnetic field (21). In this model, complex next-nearest-neighbor hopping breaks time-reversal symmetry, leading to a quantized Hall response without net magnetic flux. Haldane's model describes spinless fermions and serves as a foundational theoretical construct. Building on this concept, Kane & Mele (22) introduced the quantum spin Hall (QSH) insulator by incorporating spin–orbit coupling into a graphene-based model. This system, which can be viewed as two time-reversed copies of the Haldane model corresponding to opposite spin sectors, preserves time-reversal symmetry and exhibits a topologically nontrivial insulating phase. The QSH effect was subsequently observed in HgTe quantum wells (23, 24), providing the first experimental realization of a 2D topological insulator. Three-dimensional topological insulators provide a path to achieving the IQHE at zero magnetic field through time-reversal symmetry breaking and gap opening at the surface Dirac point (25, 26). This phenomenon, known as the quantum anomalous Hall effect (QAHE), was experimentally realized in 2013 in magnetically doped topological insulator thin films (27).

Unlike the IQHE, which can be understood within a single-particle framework, the FQHE fundamentally relies on strong electron–electron interactions (28). Although the formulation of the many-body Chern number does not need a magnetic field (20), it remained unclear whether the FQHE could be realized without an external magnetic field. Initial theoretical efforts investigated this possibility in various contexts, including spin systems (29), periodic lattice potentials (30), and synthetic optical lattices (31–35). A major breakthrough came in 2011, when several theoretical works firmly established the possibility of a zero-field FQHE, also referred to as the fractional quantum anomalous Hall effect (FQAHE). Several lattice models were proposed to realize a flat Chern band—a Bloch band with flat dispersion and nonzero Chern number (36–38)—and the existence of the FQHE was firmly established through exact diagonalization studies (38–40). The resulting phase of matter is named a fractional Chern insulator (FCI) (36–41). Most of these early models (36–40) focused on spinless fermions, whereas Reference 41 extended the analysis to spinful models and proposed the bilayers of transition metal oxides as a viable material platform. Despite their differences, a common theme has emerged: The realization of the FQAHE hinges on engineering a flat Chern band, which simultaneously provides the three essential ingredients—nontrivial topology, strong electronic interactions, and suppressed kinetic energy.

Despite these early theoretical advances, the search for a material realization of the FQAHE continues. The emergence of moiré superlattices in layered 2D materials (42–44) has opened up a versatile platform for engineering flat electronic bands (45–48). A prominent example is the discovery of unconventional superconductivity in magic-angle twisted bilayer graphene (MATBG), which highlights the potential of moiré systems to host novel correlated phases (48). Beyond superconductivity, these systems have also revealed emergent phenomena such as orbital magnetism and the QAHE, particularly when MATBG is aligned with a hexagonal boron nitride (hBN) substrate (49, 50). They indicate that not only can the moiré bands be made flat but also they can be topologically nontrivial as well. When subjected to a magnetic field, Landau fan diagram measurements revealed fractional slopes at fractional fillings of the moiré unit cell, indicating the presence of interaction-driven topological states. Analysis based on the Středa formula has identified field-induced FCI states in bilayer graphene/hBN moiré systems above 30 T (51) and in MATBG above 5 T (52). Together, these results underscore the promise of moiré flat Chern bands as a viable route toward realizing the FQAHE.

In 2023, the long-sought FQAHE—fractional quantization of Hall resistance at zero magnetic field—was experimentally realized in two different material systems: twisted $MoTe_2$ bilayer ($tMoTe_2$) (53) and rhombohedral pentalayer graphene aligned with hBN (54). In the following, we review their respective material properties, outline the experimental phenomenology of FQAHE, and discuss future research directions.

2. MOIRÉ BILAYER $MoTe_2$

2.1. Modeling

In $tMoTe_2$, the moiré superlattice generated by a small interlayer twist intertwines spin-valley locking, lattice reconstruction, and topology to produce narrow valence minibands with nonzero Chern numbers. Below, we discuss the theoretical framework in modeling the $tMoTe_2$, the emergence of FQAHE, and the potential of hosting nonabelian states.

2.1.1. Moiré Hamiltonian of R-stacked homobilayer. The pioneering theory work in Reference 55 reveals a time-reversed pair of flat Chern bands and QSH insulator in $tMoTe_2$. The topology arises from the layer pseudospin skyrmions (55), which lead to spatially dependent Berry curvature and, thus, effective magnetic fields (56, 57). Below, we describe them in detail.

In twisted bilayer transition metal dichalcogenide (TMD) the stacking order—either R-type (i.e., near 0-deg twist angle) or H-type (i.e., near 60-deg twist angle) (58, 59)—plays a crucial role in determining the nature of interlayer interactions and the resulting electronic structures (60, 61). For frontier moiré valence bands, the interlayer electronic coupling depends globally on the spin configurations, as dictated by the spin-valley locking, and locally on interlayer stacking

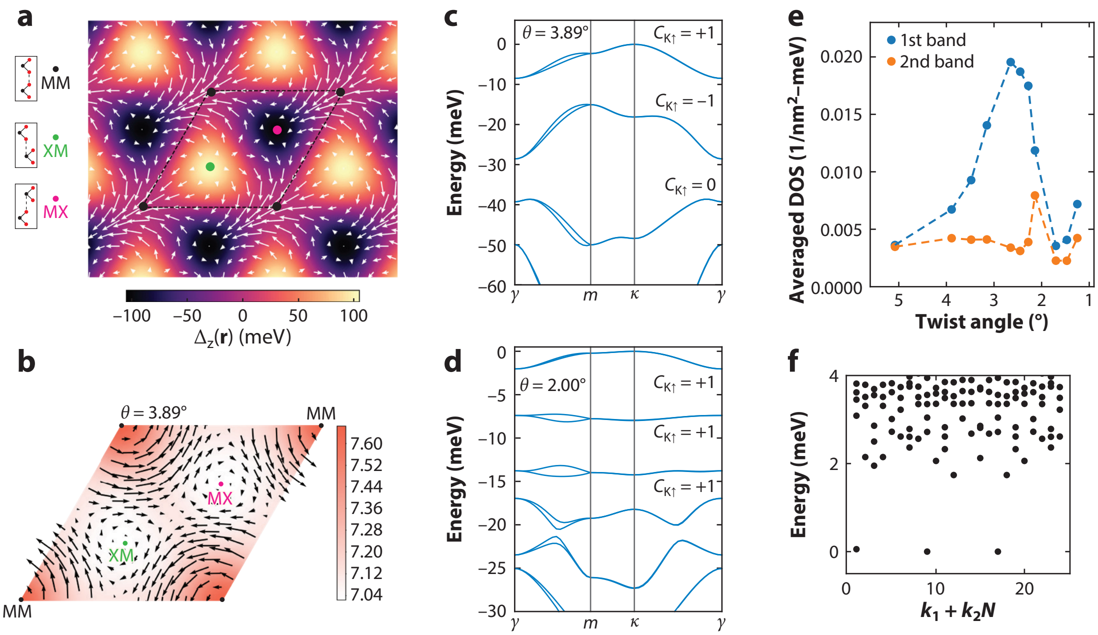

Figure 1

Theory of fractional Chern insulators in $tMoTe_2$ bilayer. (*a*) Layer pseudospin textures in $tMoTe_2$. MM/XM/MX denotes the stacking where the metal/chalcogen/metal atoms of the top layer are directly above the metal/metal/chalcogen atoms of the bottom layer, respectively. (*b*) In-plane atomic displacement (*arrows*) and interlayer distance (*color*) in a moiré unit cell due to reconstruction. The maximal in-plane atomic displacement is 0.32 Å. (*c*,*d*) Moiré miniband structures for K valley calculated from density functional theory at 3.89 deg and 2.00 deg, respectively. Chern numbers for the three topmost bands are labeled. (*e*) Calculated averaged DOS, defined as the number of electronic states per valley within the energy window of the first and second moiré band over a unit area, as a function of the twist angle. (*f*) The many-body spectrum, calculated by exact diagonalization in 3.89-deg $tMoTe_2$, as a function of total crystalline momentum for full valley polarization at $\nu = -2/3$. Panels *a*–*d* adapted from Reference 64 (CC BY 4.0). Panel *f* adapted with permission from Reference 65; copyright 2024 American Physical Society. Abbreviations: DOS, density of states; $tMoTe_2$, twisted $MoTe_2$.

configuration. In R-stacked bilayers, the interlayer hopping is generally allowed between the like-spin bands near valence band maximum (VBM), whereas in H-stacked bilayers, such hopping is suppressed owing to spin mismatches between unlike-spin bands at VBM. We therefore focus on the R-stacked twisted bilayer. Within the continuum model, the effective Hamiltonian for the K-valley electrons is given by (55)

$$\mathcal{H}_K^{\uparrow} = \begin{pmatrix} -\frac{\hbar^2(\boldsymbol{k}-\boldsymbol{K}_b)^2}{2m^*} + \Delta_b(\boldsymbol{r}) & \Delta_T(\boldsymbol{r}) \\ \Delta_T^{\dagger}(\boldsymbol{r}) & -\frac{\hbar^2(\boldsymbol{k}-\boldsymbol{K}_t)^2}{2m^*} + \Delta_t(\boldsymbol{r}) \end{pmatrix}, \tag{1}$$

where $\Delta_{b/t}(\boldsymbol{r})$ and $\Delta_T(\boldsymbol{r})$ are the intra- and interlayer moiré potential, respectively. Due to the spin-valley coupling, the band edge at each valley is spin split, and opposite valleys carry opposite spins as required by time-reversal symmetry (62, 63). The continuum Hamiltonian for the K' valley spin-down electrons can be obtained by applying time-reversal symmetry to $\mathcal{H}_K^{\uparrow}$, resulting in moiré bands with opposite Chern numbers. The moiré potential can be represented as an effective layer pseudospin magnetic field $\boldsymbol{\Delta}(\boldsymbol{r}) = (\mathrm{Re}\,\Delta_T, -\mathrm{Im}\,\Delta_T, \frac{\Delta_b-\Delta_t}{2})$. It has been shown that $\boldsymbol{\Delta}(\boldsymbol{r})$ gives rise to layer-pseudospin skyrmion textures in real space (55), which describes the relative contribution of each layer to the local electronic wavefunction (**Figure 1*a***).

As a result, the holes in top moiré valence bands experience an effective magnetic field (56, 57), which could be mapped to an effective spin–orbit coupling term acting among localized orbitals, realizing the Kane–Mele quantum spin-Hall model at small twist angles (55). From the local stacking approximations, these frontier orbitals have been found to localize at two high-symmetry regions (MX and XM) in a single moiré supercell. The MX and XM orbitals are connected by an in-plane C_2 symmetry and form the two sublattices of a honeycomb structure. Thus, the R-stacked bilayer provides a natural platform for exploring both real-space skyrmion textures and momentum-space topological phases, making it a promising candidate for studying coupled topological and correlated phenomena in the case of strong electron–electron interactions.

One route toward enhanced many-electron interaction is to engineer a flat band that quenches the kinetic energy of electrons (46). Of particular interest are interaction-induced topological phases at partial filling of the spinful topological flat bands in twisted bilayer TMD. Based on continuum model (55) and first-principles moiré band structure calculations, the flat Chern bands could have relatively uniform Berry curvature, suggesting a resemblance with the LLL that is conducive to FQAHE (66). Exact diagonalization studies on $tMoTe_2$ (67) and WSe_2 (68) further show that Coulomb interaction can induce a spontaneously and fully spin/valley polarized state at $\nu \leq 1$ (ν is the number of holes in a moiré unit cell), and in this setting, FQAHE can emerge at fractional fillings of the flat Chern band of a given valley, leading to FCI with spontaneous ferromagnetism. Building on this foundational work (55), these early theoretical studies (66–68) suggest a rich phase diagram of interaction-induced phases in twisted bilayer TMD, including quantum anomalous Hall (QAH) and fractional quantum anomalous Hall (FQAH) states as well as other correlated insulating and metallic states to be discussed below.

2.1.2. Moiré lattice reconstruction and flat Chern bands. In moiré superlattices, the low-energy band dispersion is determined by the periodic moiré potential that arises from the interplay of lattice reconstruction, interlayer coupling, and various electrostatic interactions. In particular, for R-stacked twisted bilayer TMD and boron nitride, the absence of inversion symmetry within each layer and the in-plane mirror symmetry between adjacent layers allow finite piezoelectric and ferroelectric polarizations, respectively (69, 70). Compared with twisted bilayer graphene, this polarization results in an additional contribution to the moiré Hamiltonian (i.e., an out-of-plane effective magnetic field acting on layer pseudospin) entirely due to reconstruction (71, 72).

Furthermore, the moiré lattice reconstruction is twist-angle dependent, which is negligible at large twist angle, but gradually enhances until forming large domains of high-symmetry, low-energy stacking configurations (i.e., XM and MX) (**Figure 1*b***). During this process, the competition between piezoelectric and out-of-plane ferroelectric polarization leads to a polarization reversal at these high-symmetry positions (64). This causes a change in sign of the effective magnetic field and reversal in the real-space skyrmion number and, consequently, a change in the Chern number of the topmost moiré valence band observed in $tMoTe_2$ at about 3 deg to 4 deg and twisted WSe_2 at about 1 deg (53, 73–75).

The complex reconstruction poses significant theoretical and computational challenges. Machine-learning assisted first-principles calculations have been employed to overcome the scaling in computational cost [$O(N^3)$ in plane-wave density functional theory calculations with N corresponding to the size of moiré cell]. Machine-learning force fields for $MoTe_2$ and WSe_2 have been constructed using training data from larger twist angle moiré cell or various bilayer unit-cell configurations (64, 76, 77). The trained force field can be used to predict reconstruction patterns at smaller twist angle moiré cells.

The unique reconstruction of the moiré lattice also influences band flatness, resulting in a flat Chern band at twist angles near 3 deg in $tMoTe_2$ (**Figure 1*c***) (64, 65, 76, 78). The flat Chern band provides a platform for exploring exotic quantum phases, including zero-field FCIs and higher Landau-level analogs in the absence of a magnetic field (**Figure 1*d***), as we discuss next. The ability to engineer such bands via lattice relaxation and polarization effects also provides guidance for designing intertwined topological and correlated states in other moiré platforms.

2.1.3. FQAHE at fractional filling.

In $tMoTe_2$, doping the flat band can result in a ferromagnetic ground state due to interaction-driven spontaneous valley polarization (see Section 2.2 below). At integer fillings, twisted bilayer TMDs have been predicted to stabilize as a Chern insulator with QAH conductance, accompanied by spontaneous time-reversal symmetry breaking (55, 66, 67).

At fractional fillings, the interplay between band topology and strong electron–electron interactions gives rise to a rich phase diagram, including competing states such as ferromagnetic metals (67, 68), generalized Wigner crystals (68), and zero-field FCIs (or FQAHE states) (67, 68, 78–81). Exact diagonalization studies on first-principles-derived Hamiltonians for $tMoTe_2$ have revealed robust zero-field FCI states near $\nu = -2/3$ for relatively large twist angles around 3 deg to 4 deg (65, 76, 78), coinciding with experimental observations that we discuss later (**Figure 1*f***).

The stability of FCI states critically depends on the flatness and Chern number of the underlying bands, as well as the band mixing effects (76, 82, 83). First-principles calculations incorporating lattice reconstruction have shown that twist-angle-dependent moiré potential variations enhance band flatness and uniformity of Berry curvatures, promoting FCI formation under near-ideal conditions at optimal angles (∼3.5 deg) (65). Numerical studies using exact diagonalization further confirm that these bands support FCI states at $\nu = -2/3$ with significant energy gaps, whereas $\nu = -3/5$ states remain accessible with increasing interaction strength (65, 84).

2.1.4. Composite Fermi liquid.

At half-filling ($\nu = -1/2$) of the topological valence band in $tMoTe_2$, a unique phase emerges: the composite Fermi liquid (CFL). CFL is a non-Fermi liquid formed by composite fermions, originally discovered in 2D electron gas systems under strong magnetic fields. Despite the presence of strong magnetic fields, the effective magnetic field experienced by the composite fermions vanishes at exactly half filling of the LLL. Unlike conventional Fermi liquids, the CFL consists of charge-neutral composite fermions formed by binding two flux quanta to electrons. This phase exhibits metallic behavior but lacks Landau quasiparticles.

Numerical simulations, including exact diagonalization and density matrix renormalization group studies, have provided robust evidence for the CFL in $tMoTe_2$ at zero magnetic field (85–87). These studies reveal that the many-body spectrum at half-filling exhibits momentum-space features consistent with a composite Fermi sea. Remarkably, these signatures align closely with those observed in the half-filled Landau level under strong magnetic fields, but here they arise purely from the intrinsic properties of the Chern band.

Similar to the presence of FQAHE at $\nu = -2/3$ filling, the formation of the CFL at half filling is facilitated by several factors unique to $tMoTe_2$. The small bandwidth of the nearly flat topological bands suppresses kinetic energy, allowing electron–electron interactions to dominate, as we discussed in previous sections. Additionally, the Chern band's quantum geometry, characterized by near-ideal Berry curvature and Fubini–Study metric, promotes the stability of the CFL. These features enable the mapping of the half-filled Chern band to a framework analogous to the half-filled LLL, in which composite fermion theory has been extensively developed.

2.1.5. Nonabelian physics.

A key discovery from the first-principles calculations is that the low-energy moiré electronic structures of $tMoTe_2$ carry multiple isolated flat minibands of $C = 1$, with approximately equal energy spacing at close to a 2-deg twist angle (**Figure 1*d***). This suggests that the analogs to Landau levels exist even beyond the lowest moiré band. Strikingly, the second band can exhibit essential quantum geometric signatures that closely resemble those of the first excited Landau level (1LL), including a large, nearly uniform Berry curvature and trace condition of the Fubini–Study metric.

Through exact diagonalization calculations based on continuum models or Wannier-function-based approaches, $tMoTe_2$ has been demonstrated to become a nonabelian even-denominator FCI at a filling factor of $\nu = -3/2$ (88–92). These studies, performed on a torus geometry, unveil a many-body ground state with a sixfold near-degeneracy for even total particle number in the half-filled second moiré band, and a twofold near-degeneracy for odd particle numbers. The ground-state degeneracy obtained in the calculated many-body spectrum is consistent with the nature of Pfaffian or anti-Pfaffian states.

The significance of these predictions is twofold. First, they show that nonabelian FQAH states, which were previously thought to require a half-filled 1LL under high magnetic fields, can be realized in a lattice system without any external field in $tMoTe_2$. Second, from a practical standpoint, the ability to engineer such states in moiré materials may permit more accessible platforms for future experiments on nonabelian anyons and braided excitations, which lie at the heart of topological quantum computing.

2.2. Experiment

In this section, we summarize the experimental progress in realizing the FQAHE in $tMoTe_2$. We first describe the observation of spontaneous ferromagnetism by magnetic circular dichroism measurements. Signatures of FCI states were identified by comparing optically detected fan diagrams with Středa formula analyses. We then present transport evidence of fractionally quantized anomalous Hall signal and a zero-field CFL state supported by complementary optical measurements. The microscopic properties of the FCI states are further elucidated through scanning probe studies. Finally, we discuss recent experimental advances in exploring the physics of higher-energy flat Chern bands.

2.2.1. Electrically tunable spontaneous ferromagnetism. An indispensable ingredient for the FQAHE is spontaneous time-reversal symmetry breaking, provided by the spontaneous ferromagnetic order. This was initially observed in $tMoTe_2$ in rhombohedral stacking with a twist angle between 3 deg and 4 deg (93). Later efforts expanded the range of the twist angle to between 2 deg and 4.2 deg (94–96). Using reflective magnetic circular dichroism (RMCD) measurements, ferromagnetism in a large phase space of hole doping and electric fields were identified (**Figure 2*a***). The observed ferromagnetism has strong doping-dependent cohesive fields (H_c) and Curie temperature (T_c). At moiré filling factors ν of -1 and $-2/3$, H_c and T_c are about 100 mT and 14 K, and 25 mT and 4.5 K, respectively (93). At fixed doping, an electric field can control the ferromagnetic properties and eventually suppress the ferromagnetism above a critical value. The critical electric fields are doping dependent, peaking at $\nu = -1$ and $-2/3$ (**Figure 2*b***). Despite the fact that the exact ground state at large electric field remains to be determined, initial measurements found negative Curie–Weiss temperature, suggesting antiferromagnetic interactions (93).

As described in the theory section, at twist angle of 3 deg and above, the moiré frontier bands arise from orbitals localized at the two energy-degenerate high-symmetry regions (MX and XM) in a moiré unit cell. These moiré localized orbitals from these two sublattices have significant wavefunction overlap inside and among adjacent moiré cells. The direct Coulomb exchange interactions between these carriers give rise to the Stoner-type, valley-polarized ferromagnetism upon doping. Because the moiré sublattices form the basis of the layer pseudospin, applying a perpendicular electric field breaks the degeneracy of the moiré orbitals and, thus, the layer pseudospin. This effectively changes the superlattice geometry from honeycomb to triangular,

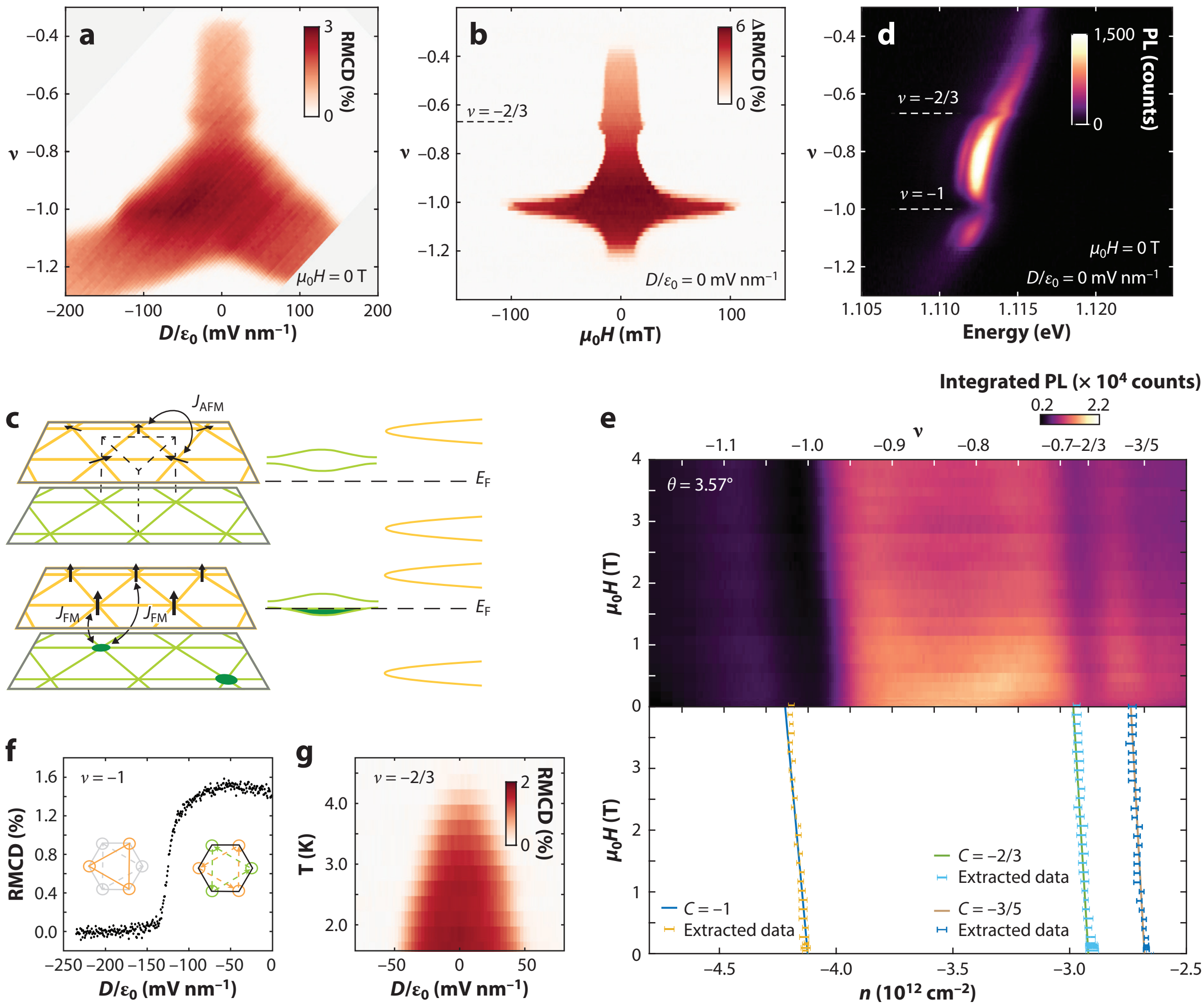

Figure 2

Electrically tunable spontaneous ferromagnetisms and optical sensing of zero-field FCI states. (*a*) RMCD signal versus filling factor ν and electric field D of $tMoTe_2$. Data are taken at zero magnetic field and a temperature of 1.6 K. The nonvanishing signal represents the ferromagnetic phase. (*b*) Difference of RMCD sweeps between forward and backward magnetic fields, ΔRMCD, versus ν and magnetic fields. Clear enhancement of cohesive fields at $\nu = -1$ and $\nu = -2/3$ is observed. (*c*) Schematic illustration of the interplay between on-site Coulomb interaction and charge transfer energy, which gives rise to the revival of ferromagnetism of a doped Mott insulator at large electric field. (*d*) PL intensity plot versus ν and photon energy, where PL quenching corresponds to the formation of correlated insulating states. (*e*, *upper panel*) Spectrally integrated PL intensity versus magnetic field and ν (or carrier density n), that is, an optical Landau fan diagram. (*e*, *lower panel*) Wannier diagram corresponding to three Chern insulator states with $C = -1$, $-2/3$, and $-3/5$, respectively. (*f*) RMCD signal at $\nu = -1$ versus electric field, demonstrating an electric field–driven magnetic phase transition concurrent with the change in superlattice geometry from honeycomb to triangular (*insets*). (*g*) Ferromagnetic phase diagram versus temperature and D at $\nu = -2/3$. Panels *a*, *b*, and *d*–*g* adapted with permission from Reference 73. Panel *c* adapted with permission from Reference 93. Abbreviations: PL, photoluminescence; RMCD, reflective magnetic circular dichroism; $tMoTe_2$, twisted $MoTe_2$ bilayer.

which is responsible for the observed electric field–induced magnetic phase transition from a ferromagnet to a putative antiferromagnet. With full-layer polarization, experiments also observed the revival of ferromagnetism as hole doping increases beyond $\nu = -1$. This is due to the competition between on-site Coulomb interaction energy U and charge transfer energy Δ between the layers (**Figure 2*c***). When $\Delta < U$, the additional holes can redistribute to the opposite layers and mediate the ferromagnetic exchange interactions between the majority holes located in the triangular lattice. Anderson et al.'s (93) findings suggest that t$MoTe_2$ offers a powerful platform for investigating a variety of magnetic phases with strong tunability.

2.2.2. Spectroscopic evidence of the zero-field fractional Chern insulator. $MoTe_2$ is unique in that it is a direct bandgap semiconductor in the bilayer form (93, 97, 98). This is distinct from other isostructural TMD semiconductors (e.g., MoS_2, WSe_2, $MoSe_2$, WS_2), whose bilayers are indirect bandgap. This direct bandgap feature enables strong photoluminescence (PL) from charged valley excitons (i.e., trions) as an effective probe of magnetism and Chern insulator states. Doping-dependent PL was first carried out to establish the formation of correlated insulators at certain moiré fillings (73). Suppressed trion PL at both integer and fractional filling ν is observed (**Figure 2*d***). Because the formation of trion requires extra carriers, trion PL intensity suppression implies the formation of correlated insulating states, which gaps the Fermi surface and impedes the trion formation. The combined trion PL and RMCD results established the correlation-induced ferromagnetic insulating states at both integer and fractional hole filling of the moiré flat bands, which are candidates of QAH states.

Making good metal contacts to 2D semiconductors is a known challenge in the community. The initial signature of the zero-field FCI states was then achieved by measuring the fan diagram of the ferromagnetic insulating states through trion PL (**Figure 2*e***) (73). The fan diagram yields the topological invariants associated with the gapped states via the Středa formula $C = \phi_o \frac{\partial n}{\partial B}$. Here, C is the Chern number, n is the carrier density that corresponds to the gapped state, and B is the magnetic field. As shown in **Figure 2*e***, three dispersive features are obtained at filling factors -1, $-2/3$, and $-3/5$. Compared to the Středa formula, these characteristics provide evidence of the QAH states with Chern number -1, $-2/3$, and $-3/5$. By fabricating a sensing layer WSe_2 in proximity to the t$MoTe_2$, the $-2/3$ zero-field FCI state was later confirmed via measurement of the optical reflectance of the WSe_2 exciton (74). As described above, the application of the vertical electric field leads to the ferromagnetic phase transition (**Figure 2*f*,*g***), which should accompany the QAH phase transition. The observed ferromagnetic (FM) state at $\nu = -2/3$ also has a large T_c value (**Figure 2*g***) (73). As shown below, this leads to zero-field FCI states with large energy gaps.

2.2.3. Transport measurement. Establishing zero-field FQHE must require transport measurement of Hall signal (R_{xy}), and direct evidence would be fractionally quantized R_{xy} with vanishing longitudinal resistance R_{xx} at zero magnetic field. Several schemes have been developed in the community to achieve good metal contacts with TMDs (99, 100). However, these schemes are not feasible for accessing the phase space with vanishing electric fields across the sample, where layer pseudospin skyrmions form. To address this challenge, Reference 53 employed local gates for each metal contact, enabling reasonable contact resistance (tens of kiloohms) for t$MoTe_2$. **Figure 3*a*,*b*** shows the R_{xy} and R_{xx} versus doping and electric fields, respectively. The parameter space with suppressed R_{xx} and corresponding enhanced R_{xy} highlights the QAH phases. Integer QAH states are observed near $\nu = -1$, which remains quantized at about 6 K, suggesting its large energy gap. Zero-field FCI states are observed at $-2/3$ and $-3/5$ fillings, with the critical temperature of quantization near 2 K. The integer and nearly quantized $-2/3$ QAH states were also later confirmed at lower temperature with a different contact design (105). These QAH states can

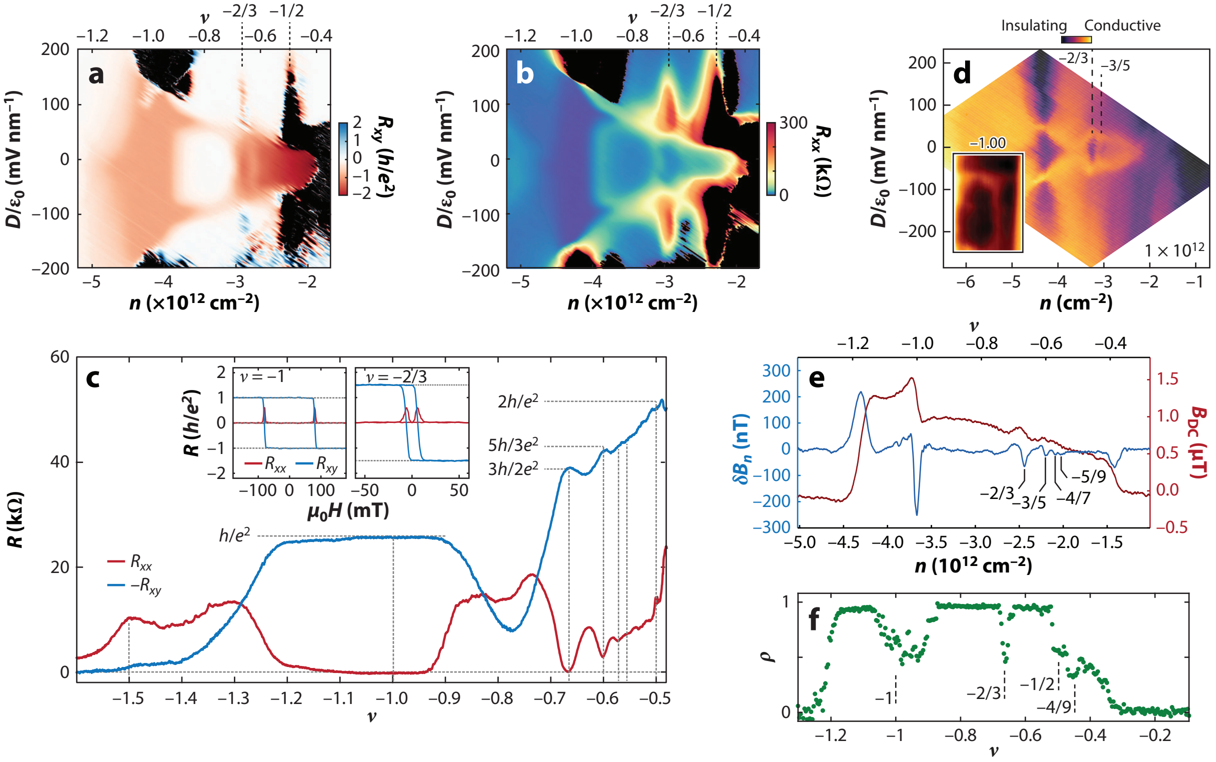

Figure 3

Transport and scanning probe measurements of FQAHE in twisted $MoTe_2$ bilayer. (*a*) Hall (R_{xy}) and (*b*) longitudinal (R_{xx}) resistance as functions of electric field D and carrier density n at 100 mK. Data taken with permission from Reference 53. (*c*) Symmetrized R_{xx} (*red*) and antisymmetrized $-R_{xy}$ (*blue*) at $B = \pm 100$ mT versus ν below 30 mK. Jain sequence $-\frac{p}{2p-1}$ ($p = 2, 3, 4, 5$) FCI states are observed. (*c*, *inset*) Measurements of R_{xx} and R_{xy} as functions of magnetic field for the $C = -1$ and $-2/3$ QAH states. Data taken with permission from Reference 101. (*d*) The MIM-Im signal as a function of displacement field and carrier density at 1.5 K. (*d*, *inset*) Spatial map of MIM-Im at the QAH state, showing the conducting edge state with an insulating bulk. Data taken from Reference 102. (*e*) DC (*red*) and AC (*blue*) measurements of local magnetic field by nanoSQUID versus ν at 1.6 K, which reveals abundant FCI states. Data taken with permission from Reference 103. (*f*) Degree of circular polarization ρ of trion photoluminescence at 1.6 K versus ν. Drops are visible in ρ around $\nu = -1$, $-2/3$, and $-1/2$, as well as in an additional dip consistent with the $\nu = -4/9$ Jain state. Data taken with permission from Reference 104. Abbreviations: FCI, fractional Chern insulator; FQAHE, fractional quantum anomalous Hall effect; MIM-Im, microwave impedance microscopy–imaginary; QAH, quantum anomalous Hall.

transition into topological trivial insulating states by the application of electric fields, which offer a powerful platform to investigate phase transition between different types of correlated (topological) states. In addition, the ability to switch off the chiral edge current and transition into an insulating state can be potentially useful for the realization of topological transistors.

In the initial observation of FQAHE, although R_{xy} is quantized, R_{xx} remains finite (~5–10 kΩ) (**Figure 3*a*,*b***). This dissipative behavior is likely due to sample quality, similar to the landmark discovery of FQHE in 1982 (2). Rapid progress has been made in improving $MoTe_2$ crystal. This leads to the observation of the nondissipation $-2/3$ zero-field FCI state (**Figure 3*c***) (101, 106). Additional Jain sequence of FCI states are also observed, although R_{xx} remains finite, suggesting a possibility for further improvement in sample quality. Using this high-quality device, the thermal activation gap of the $-2/3$ FCI state was investigated versus magnetic field B (101). Unlike FQHE states with an energy gap increasing as $\sqrt{B}$, and the field-induced FCI in which the energy gap increases with B (52, 107), the thermal activation gap of the FCI states drops rapidly as the magnetic field increases and then plateaus at a higher field. This observation is attributed to the two-gap behavior. At zero magnetic field, spin-fluctuation/magnetic domain dominated transport behavior near Curie temperature. As magnetic field increases, the spin fluctuation is suppressed and eventually frozen, giving rise to the intrinsic FCI gap. Note that the energy gap of both integer and fractional QAH states is quite high, which is due to the strong carrier–carrier interactions from close carrier separation on the order of moiré wavelength as well as reduced screening effect in the atomically thin limit.

2.2.4. Scanning probe measurements. An intrinsic property of FCI is the bulk-boundary correspondence, i.e., edge conduction with insulating bulk states. This property was investigated by a light-coupled scanning microwave impedance microscopy (MIM) technique (102). An open challenge for scanning probe measurements of local conductance is the screening of the metallic tip by the top gate. This challenge is overcome by utilizing a monolayer WS_2 as a top gate. Monolayer WS_2 is a semiconductor. However, under light illumination, photoexcited carriers in WS_2 are mobile enough to function as a gate while not fully screen the tip. Scanning MIM measurements of the bulk states as a function of doping and electric field resembles the FQAH phase diagram in transport (**Figure 3*d***). At small electric field, there are local conductivity minimums at $\nu = -1, -2/3$, and $-3/5$, corresponding to the integer and FCI states. At large electric field, the conductivity minimum is also observed at $\nu = -1$ and $-2/3$, which suggests a correlated insulating state. There is a metallic regime near critical electric fields, which corresponds to the gap closing during the electric field–induced Chern insulator to correlated insulator phase transition. By scanning the MIM tip across the sample, a conductive edge state with insulating bulk is visualized at Chern insulator states (**Figure 3*d***, *inset*). Furthermore, the edge states vanish for the correlated insulator at large electric field at fixed doping (e.g., at $\nu = -2/3$), supporting the idea that the edge conducting channels are due to the formation of FCI states rather than charge accumulation at the sample edge.

QAH states and associated magnetic properties have also been probed via a scanning nanoSQUID (103). Scanning nanoSQUID is a sensitive local measurement of stray magnetic fields. The experiment reveals a ferromagnetic phase diagram nearly identical to magnetic circular dichroism measurements. Because the orbital magnetization varies as the chemical potential is swept through the Chern insulator gap, both DC and AC measurements show several Chern insulators (**Figure 3*e***). Remarkably, the thermal dynamic gap of the $-2/3$ state was measured to be about 7 meV. A nanoSQUID spatial map also reveals significant moiré disorder in the exact device used in the transport measurement (53). However, because of the very large gap of the FCI states, transport measurement can still observe fractionally quantized Hall resistance despite the existence of moiré disorder.

2.2.5. Signature of composite Fermi liquid state. An intriguing observation in the transport measurement of the 3.7-deg twisted sample is that the anomalous Hall signal R_{xy} is approximately $2h/e^2$ at half filling and varies linearly as ν, suggesting the state is compressible (**Figure 3*b*,*c***) (53, 101). In the entire regime, R_{xx} is finite (5–10 kΩ). In fact, the behavior of the state resembles that observed near half filling of the LLL in a 2D electron gas at high magnetic fields (108). In the latter case, the state was found to be a CFL state (28, 109–113). Although the evidence so far does not prove a zero-field CFL state, numerical calculations of the exact $MoTe_2$ system demonstrated a CFL state at half filling, as we discussed in Section 2.1.4 (85, 86).

An additional support to the zero-field CFL state is provided by the trion sensing measurement (104). The trion PL intensity and energy do not show, respectively, appreciable suppression and shift near half filling, which is consistent with the compressible nature of the CFL state.

By performing helicity resolved measurements, the degree of circular polarization (ρ) is near unity within the ferromagnetic phase at doping without the formation of QAH states. However, at both integer and fractional QAH states, and near $-1/2$ filling, ρ is strongly quenched (**Figure 3*f***). Temperature-dependent measurements show ρ increases as temperature increases, and approaches unity at a critical temperature at which R_{xy} starts to deviate from quantized values, and eventually drops as temperature approaches the Curie temperature. This behavior can be explained by the local charge excitation gap (or pseudogap) of the CFL state (114). To form spin-polarized trion, the photoexcited electron–hole pair needs to bound a spin-polarized hole. However, in the CFL state, excitation of a spin-polarized hole needs to overcome the pseudogap of the CFL state (114), which thus suppresses ρ. The temperature dependence implies the thermal activation behavior of the CFL state. This interpretation is further supported by the electric field dependence. For the non-(F)QAH state, ρ is near unity at small electric field and then drops at large electric field when ferromagnetism is quenched. For the (F)QAH states or the putative CFL state, ρ is suppressed at small electric fields and revives to unity when the electric field is increased to phase transition boundary, where the gap is closed, and then drops as ferromagnetism is destroyed at very large electric field. The concurrent RMCD measurements with the presence of an excitation laser show that the signal behaves similarly for all fillings, i.e., near plateau at small electric fields, and then vanishes at large ones in which the FM state is gone. This rules out spin depolarization induced by photoexcitation as the explanation. To establish a solid Fermi surface, measurements should be performed as those done in two-dimensional electron gas, such as the surface acoustic wave and the antidot lattice (111, 112). Another possibility is to use MIM measurement with its capabilities in resolving Fermi wavevector.

2.2.6. Higher-energy Chern bands. So far, the FQAHE phase diagram of the first Chern band with partial hole filling behaves like the FQHE one in the LLL. All observed FQAHE states resemble the Jain sequence FQHE states in odd denominators. These states are expected to host abelian anyons. Certain FQHE states in higher Landau levels, such as the 5/2 state (108), are promising candidates for realizing nonabelian anyons (7, 15, 108, 115–118). Thus, a natural route to create nonabelian FCI states is to explore higher-energy moiré Chern bands beyond the first one (88–92, 119).

Experiments have been carried out to investigate higher-energy Chern bands. We separate the discussion into two categories regarding the twist angles. The first category is samples with a twist angle ranging between 2.4 deg and 4 deg. Spontaneous ferromagnetism is observed at $\nu = -3$ by RMCD measurements (94). Transport measurements reveal anomalous Hall signal R_{xy}, which is appreciable but smaller than h/e^2 and R_{xx} (94, 120) (**Figure 4*a***). At high magnetic field, quantized R_{xy} (h/e^2) and strong R_{xx} dip are observed. Combined with the fan diagram revealing the Středa slope with $|C| = 1$, the state is identified as an incipient Chern insulator state with gap opened by magnetic fields. What is interesting is that the Středa slope, i.e., the Chern number, switches sign as a function of twist angle (**Figure 4*b*,*c***). It has an opposite sign compared to the first Chern band for large twist angle and the same sign at low twist angle. The latter case is further confirmed by the observation of field-induced $|C| = 2$ Chern insulator state near $\nu = -2$ (**Figure 4*c***). The exact angle at which the sign switching happens has not been experimentally determined, but it is expected to be between 2.6 and 3 deg based on both theory (64) and available experimental data (94, 120). So far, no noticeable features at $\nu = -5/2$ have been reported. At 3/2, large R_{xx} with vanishing R_{xy} has been observed either at zero magnetic field for a large twist angle (3.7 deg) (101) or at high magnetic field for small twist angles (2.6 deg) (94). These observations suggest a topological trivial correlated insulating state at $\nu = 3/2$ within the studied twist angle range.

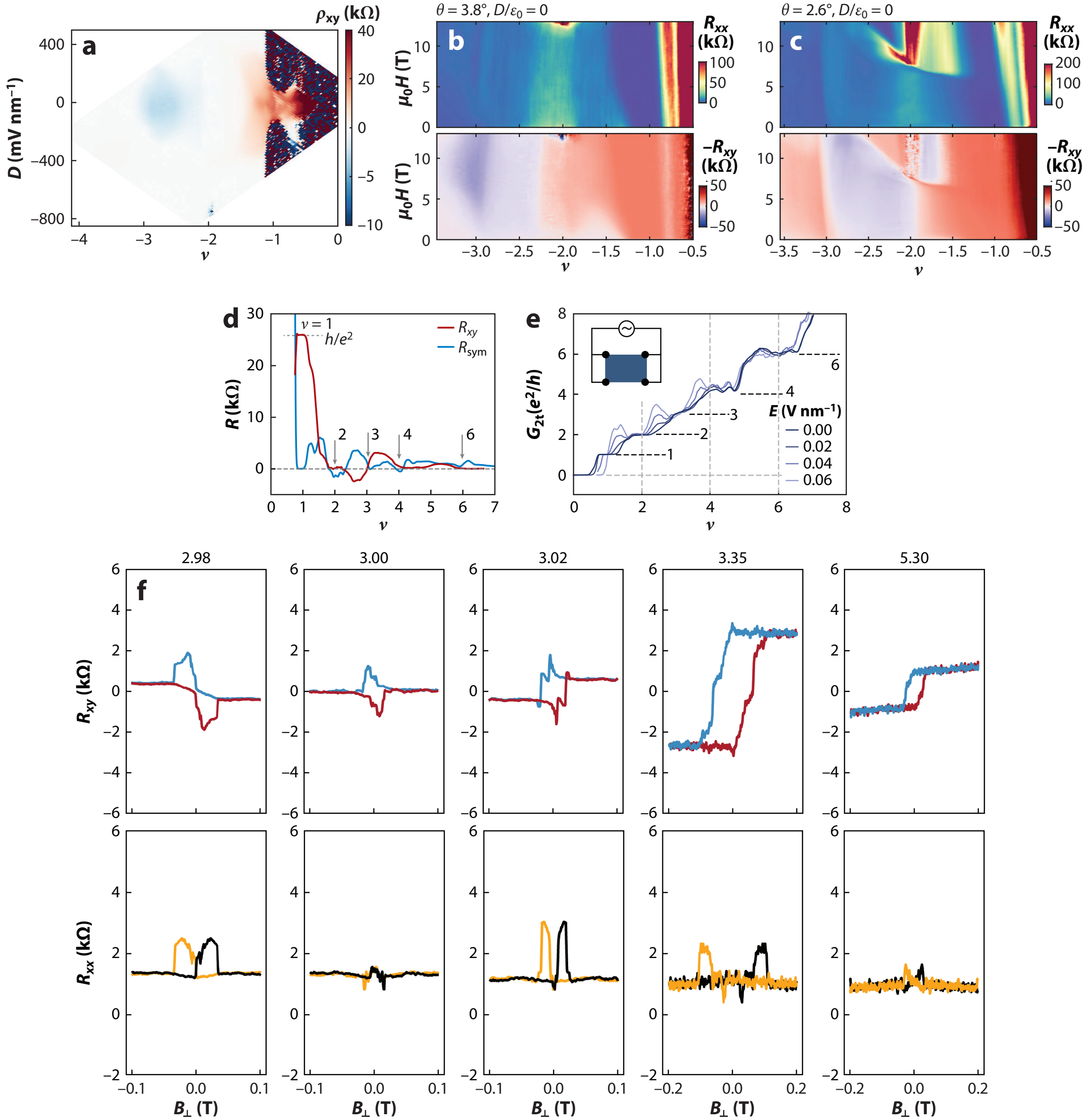

Figure 4

Topology and magnetism of the second flat Chern band. (*a*) Antisymmetrized Hall resistivity at $B = \pm 0.1$ T and 1.6 K versus ν and D for a 3.15-deg twisted device. (*b*) Landau fans of symmetrized R_{xx} (*top*) and antisymmetrized $-R_{xy}$ (*bottom*) at T of about 30 mK for a 3.8-deg device. (*c*) The same as in panel *b* for a 2.6 deg twisted $MoTe_2$ bilayer device. (*d*) Four-terminal resistance R_{sym} (*blue*, subtracting a constant resistance) and Hall resistance R_{xy} (*red*). The dashed lines denote the expected resistance around $\nu = 1, 2, 3, 4$, and 6. (*e*) Two-terminal conductance versus ν at selected electric fields. (*f*) Magnetic field dependence of R_{xy} (*top*) and R_{xx} (*bottom*) near ν of 3 (hole doping) at 20 mK. Panel *a* adapted with permission from Reference 120. Panels *b* and *c* adapted with permission from Reference 94. Panels *d* and *e* adapted with permission from Reference 121. Panel *f* adapted with permission from Reference 96.

Calculation shows the bandwidth of the second Chern band has a strong dependence on twist angle and becomes really flat near 2.1 deg (64). Initial transport measurements report zero anomalous Hall conductivity at $\nu = -3$ (**Figure 4*d***). Combined with nearly quantized two-terminal conductance (after subtracting a constant background) (**Figure 4*e***), the results are interpreted as fractional quantum spin Hall (FQSH) effect resulting from a time-reversal pair of the even-denominator 3/2-FCI (121). In addition, single, double, and triple QSH at $\nu = 2, 4$, and 6, respectively, were reported (**Figure 4*d*,*e***). These results generate great interest in the community. Both time-reversal symmetric and broken states have been proposed for the $\nu = -3$ state (88, 119, 122). Soon after, robust ferromagnetism at $\nu = -3$ in 2.1-deg twisted sample was reported by RMCD measurements (95). This shows that the state has broken time-reversal symmetry. Recently, the same group that reported FQSH performed additional measurements and observed finite R_{xy} at zero magnetic field with a small hysteresis loop (**Figure 4*f***) (96). Interestingly, R_{xy} vanishes at finite magnetic field. This result is interpreted as time-reversal symmetry broken FQSH. The exact nature of the state remains unknown. Investigations with high-quality devices are needed to rule out trivial causes, such as magnetic domains and moiré disorders known to exist in t$MoTe_2$ samples. Other techniques, such as MIM measurements to image the conducting edge with insulating bulk, would be necessary to support a QSH edge state (123). Another interesting observation from the initial report of FQSH is an R_{xx} dip with a nearby R_{xy} shoulder for ν between −1 and −2. The state was interpreted as a 3/2 FCI state (96, 121) (**Figure 4*d***). Future studies with additional devices and measurements are needed to explore this interesting feature. For instance, a fan diagram is necessary to show whether the R_{xx} dip shifts versus B field and to extract the Chern number via Středa formula analysis. Nevertheless, higher-energy Chern bands beyond the first have already shown a glimpse of promise for searching exotic FCI states.

3. GRAPHENE

3.1. Background

In addition to t$MoTe_2$, multilayer rhombohedrally stacked graphene has emerged as a powerful platform for realizing correlated and topological phenomena. In this section, we outline the basic flat band and topological properties of this system, followed by a discussion of the experimental progress in realizing FQAHE and observing its coexistence with superconductivity.

3.1.1. Tunable flat band and Berry curvature. As a crystalline form of graphite, rhombohedral stacking (**Figure 5*a***) is a metastable form that has higher energy than the Bernal stacking (124–126). It features an electrically tunable bandgap and Berry curvature (127–134). Different from $MoTe_2$, the bandgap in pristine rhombohedral graphene is zero, whereas a bandgap can be induced by applying a vertical electric field through the top and bottom gates. The essence of the band structure can be understood by a simple tight-binding picture: Electrons from the two sublattices within the same layer remain degenerate at zero energy; by hopping to the overlapped sublattice in the next layer, one of the degenerate states is pushed away from zero energy; in the N-layer rhombohedral graphene, only two states at the sublattices located at the outmost layers remain degenerate at zero energy. The two degenerate states are analogs of the dangling bonds in the Su–Schrieffer–Heeger model (135), and they develop into the two lowest-energy bands near the Fermi level. In the pristine form without gating, a bandgap can spontaneously open in the suspended (136–140) or hBN-encapsulated (141–143) configurations because of the instability of the band-touching point. By breaking the sublattice degeneracy through a gate-induced vertical displacement field D (141, 144–148), a bandgap can be opened and tuned continuously (**Figure 5*b***). Subsequently, the density of states at the band edge can be greatly enhanced at

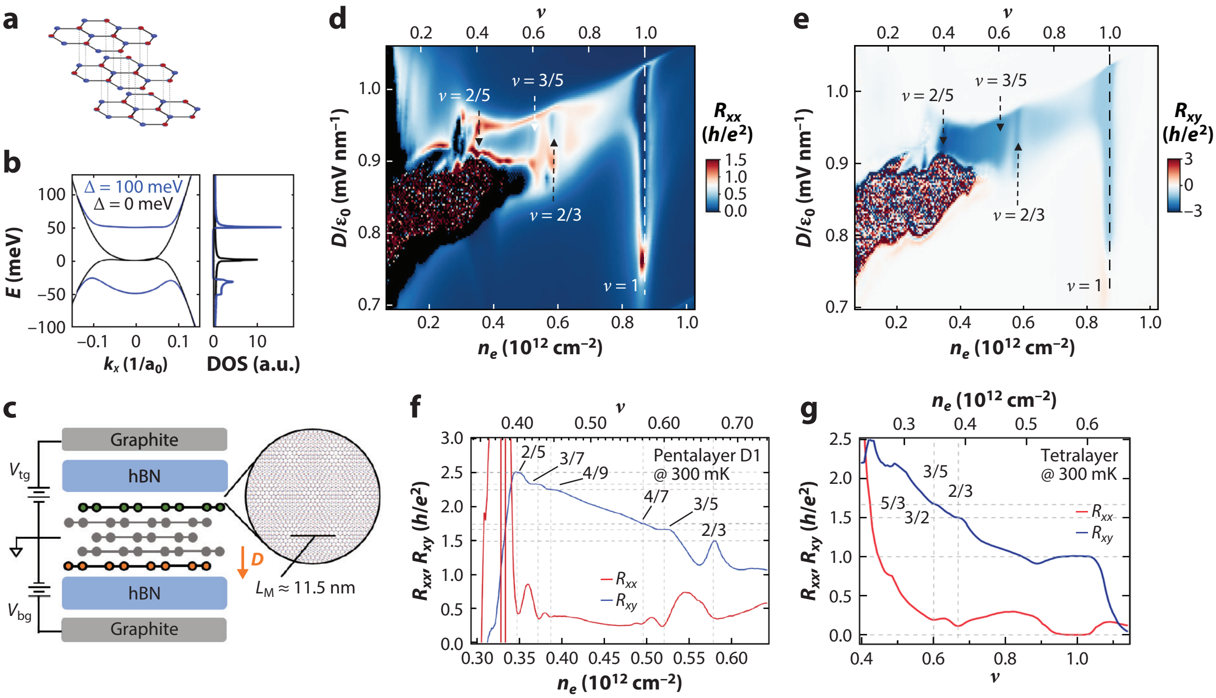

Figure 5

Observation of FQAHE in rhombohedral penta- and tetralayer graphene/hBN moiré superlattices. (*a*) Atomic structure of rhombohedral trilayer graphene. (*b*) Tight-binding calculation of the band structure and DOS in rhombohedral pentalayer graphene. Degenerate flat bands exist at interlayer potential $\Delta = 0$ meV, whereas even more flat bands (*bottom*) can be induced by $\Delta = 100$ meV. (*c*) Device structure of dual-gated rhombohedral pentalayer graphene/hBN moiré superlattice, featuring a moiré wavelength of 11.5 nm between the top-most graphene layer and top hBN flake. (*d*,*e*) R_{xx} and R_{xy} as functions of displacement field and charge density, respectively, taken at an electron temperature of 300 mK, featuring vertical stripes at integer and fractional moiré filling factors. (*f*,*g*) Line cuts of R_{xx} and R_{xy}, showing quantized plateaus and dips at fractional filling factors of the FQAHE. Panels *c*–*f* adapted from Reference 54. Panel *g* adapted from Reference 149. Abbreviations: DOS, density of states; FQAHE, fractional quantum anomalous Hall effect; hBN, hexagonal boron nitride.

optimal gate-displacement field (54), making it a potential playground of electron-correlation effects. In the full tight-binding calculation that includes all the hopping terms, the conduction and valence bands develop an asymmetry and the trigonal warping effect (141). These details contribute together with the tuning of D to the band dispersion. As the layer number is increased from 1 to 5, the density of states increases monotonically near the band edge and drives stronger electron correlation effects.

In the momentum space, the two degenerate valleys K and K' feature opposite Berry curvatures at the same band edge to conserve the time-reversal symmetry (150, 151). When the correlation effect is strong enough, the valley (and/or spin) degeneracy can be spontaneously broken owing to the exchange interaction similar to that of the Stoner mechanism of ferromagnetic metals (151, 152). Consequently, orbital magnetism and anomalous Hall effect could emerge due to the spontaneous valley polarization. The latter is the key underlying factor for the observation of the FQAHE in experiments on rhombohedral graphene/hBN moiré superlattices.

3.1.2. Moiré superlattice and Chern insulators. When placed on an hBN substrate, the lattice mismatch between rhombohedral graphene and hBN naturally leads to a moiré superlattice

(153–155). The period of this superlattice is about 15 nm at zero twist angle and can be tuned smaller at nonzero twist angle. The superlattice potential further modifies the band structure of rhombohedral graphene and can induce bandgaps at the boundary of the mini-Brillouin Zone (147, 156, 157). Consequently, in the moiré superlattices between hBN and rhombohedral tri- and tetralayer graphene, Chern insulators and integer QAHEs have been observed at the hole-doping side (158–160). The Chern numbers of such states can be as big as 4, which is greater than that in magnetic topological insulators and other moiré superlattice materials (27, 50, 161, 162), but smaller than that observed at the charge neutrality of rhombohedral pentalayer graphene/WS_2 in the absence of moiré effects (148). These high-Chern-number topological flat bands could be a playground to explore fractional electron states that are beyond what is possible in Landau levels (limited to Chern number 1), but no FCI states have been observed so far.

In general, Chern insulator gap opening at $\nu = -1$ on the hole-doping side of rhombohedral graphene/hBN moiré superlattice is expected at the single-particle level (157, 158, 163). The Chern number is expected to be the same as the layer number of graphene, although electron interaction effects could modify the Chern number depending on the effective dielectric constant used (158). These properties were not expected for the electron-doping side.

3.2. Experiment

Transport measurements on moiré superlattices formed by multilayer rhombohedrally stacked graphene and hBN have revealed several remarkable phenomena. In addition to the FQAHE, a transition to an extended quantum anomalous Hall (EQAH) state was achieved by fine-tuning experimental parameters. Strikingly, superconductivity was also observed in close proximity to the FQAHE phase boundary.

3.2.1. Transport measurement at 300-mK electron temperature. The FQAHE in rhombohedral pentalayer graphene/hBN moiré superlattice was observed directly through transport experiment (54). In the first two devices, a moiré wavelength of 11.5 nm existed between the topmost graphene layer and the top hBN flake (**Figure 5*c***), corresponding to a twist angle of 0.77 deg. At the electron-doping side, large anomalous Hall signals were observed at $D = +0.8 - 1$ V/nm, where the corresponding electrons in the conduction band are polarized to the layer farthest from the moiré superlattice rather than closest to moiré. In particular, vertical stripes in the n_e–D maps of longitudinal and transverse resistances can be seen at integer and fractional moiré filling factors (**Figure 5*d*,*e***). Quantized $R_{xy} = h/(\nu e^2)$ and corresponding dips in R_{xx} were observed at the moiré superlattice filling factors $\nu = 1, 2/3, 3/5, 4/7, 4/9, 3/7$, and $2/5$ (**Figure 5*f***). All fractional states follow the Jain sequence (109) of the FQHE. When an out-of-plane magnetic field is applied, the signatures of these integer and fractional states show dispersions with slopes that agree with the Středa formula. At half-filling, an anomalous Hall resistance of $2h/e^2$ was observed but without a plateau. The R_{xy} varies linearly with ν in the neighborhood of $\nu = 1/2$. These observations are aligned with that of the composite fermions in the fractional quantum Hall (FQH) systems at half-filling of the LLL (108–110).

Following the observations made in pentalayer graphene devices, FQAHE was also observed in tetralayer graphene (149) ($\nu = 2/3$ and $3/5$; **Figure 5*g***) and hexalayer graphene (164) ($\nu = 2/3$) through electron transport experiments. These observations indicate that the rhombohedral graphene/hBN system is a family of FQAHE materials and point to the possibility of finding FQAHE in even thicker layers of rhombohedral graphene.

3.2.2. Transport measurement at 30-mK electron temperature. One observation in the first FQAHE experiment in rhombohedral pentalayer graphene/hBN moiré superlattice was the

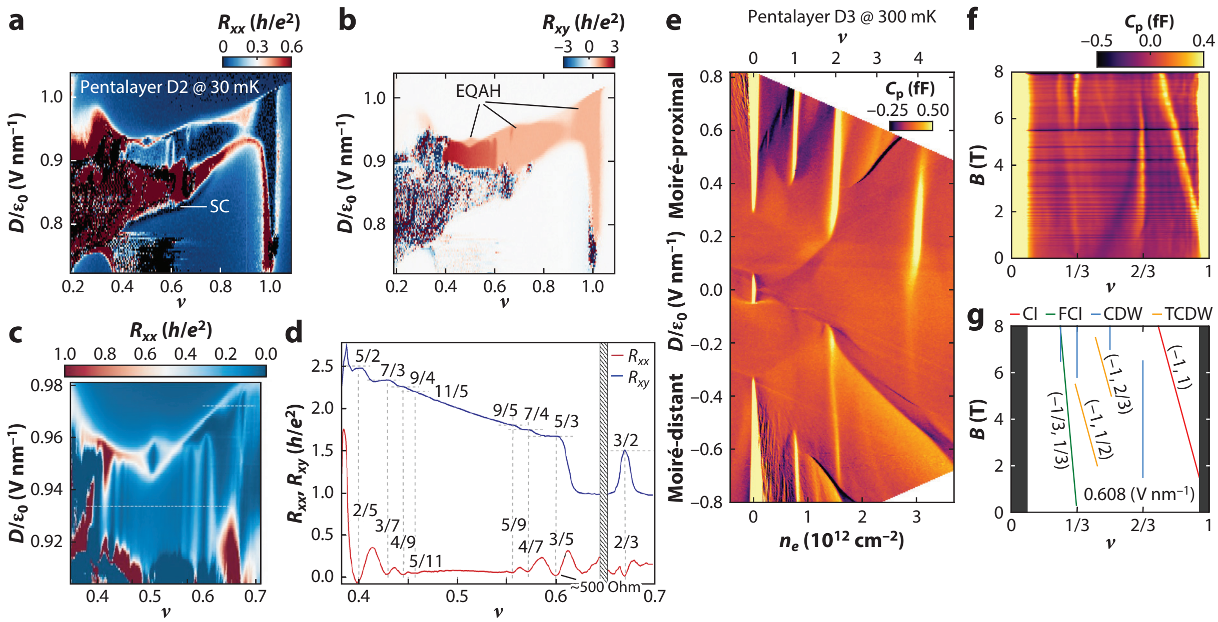

Figure 6

FQAHE and EQAH states and superconductivity at 30 mK electron temperature. (*a*,*b*) R_{xx} and R_{xy} as functions of displacement field and charge density, respectively, in pentalayer device D2, taken at an electron temperature of 30 mK. New features showing an extended region of integer QAHE (labeled as EQAH) and superconductivity (labeled as SC) coexist with FCI states. (*c*) Zoomed-in map of panel *a*, showing clear vertical stripes corresponding to 8 FCI states. (*d*) Line cuts of R_{xx} and R_{xy} along the dashed lines in panel *c*, featuring 8 FCI states with a minimal R_{xx} of 500 Ω at $\nu = 3/5$. (*e*) Penetration capacitance as a function of density and displacement field at 0 T. Bright features correspond to incompressible states. (*f*,*g*) Landau fan diagrams of the penetration capacitance at $D/\varepsilon_0 = 0.608$ V/nm, featuring an FCI state emerging from 0.2 T. Additional features include CI, CDW, and TCDW states. Panels *a* and *b* adapted from Reference 149. Panels *e*–*g* adapted from Reference 107 (CC BY 4.0). Abbreviations: CDW, charge density wave states; CI, Chern insulator; EQAH, extended quantum anomalous Hall; FCI, fractional Chern insulator; FQAHE, fractional quantum anomalous Hall effect; QAHE, quantum anomalous Hall effect; SC, superconductivity; TCDW, topological charge density wave.

large residue of $R_{xx} = 8$ kΩ at fractional fillings (R_{xx} at $\nu = 1$ was shown to be less than 5 Ω and limited by experimental noise). This is significantly higher than the values in the state-of-the-art FQH material systems. However, later in a higher-quality pentalayer graphene device made by the same group, R_{xx} down to 500 Ω was observed (149) at an electron temperature estimated to be 30 mK (**Figure 6*d***). This electron temperature was estimated based on the temperature reading when a superconducting transition happens in a graphene superconductor. At the same time, two more fractional states at $\nu = 5/11$ and 5/9 were observed. It is therefore reasonable to expect a vanishing R_{xx} of FQAHE with further efforts toward improving the device quality.

In addition to the total of 8 FCI states observed at the base electron temperature of 30 mK, three extended regions on the n_e phase diagram exhibit integer QAHE (149) at moiré filling factors other than 1, as shown in **Figure 6*a*,*b***. These states, named EQAH states, showed nonlinear voltage–current relations in both the longitudinal and transverse directions. Both the vanishing R_{xx} and quantized R_{xy} break down at a threshold longitudinal current. This behavior is reminiscent of the depinning of Wigner crystals, if one thinks the depinning electric field is in the transverse direction when a current is driven in the longitudinal direction. These EQAH states are interpreted as similar to either the re-entrant quantum Hall effect (166–171), in which an underlying integer quantum Hall insulator coexists with a Wigner crystal of holes, or the anomalous Hall crystal state that was proposed recently (172–179).

We note that the competition between the EQAH state and FQAHE at $\nu = 2/3$ is unusual and depends on the sample quality. Pentalayer device D1 and D2 make an ideal pair for comparison: They share the same hBN flakes, the same rhombohedral domain in the graphene flake before cutting, and therefore the same twist angle between graphene and hBN. During the transfer and measurement process, device D1 might have developed more disorders (as evidenced by an R_{xx} minimum of 2 kΩ) than in device D2 (an R_{xx} minimum of 500 Ω). As a result, the FCI state at $\nu = 2/3$ is replaced by the EQAH state at the base electron temperature of 30 mK in D1, whereas the same FCI state persisted in D2. A similar re-entrant quantum Hall effect has been observed in GaAs-based 2D electron gas systems, where some weak FQH states are replaced by the integer quantum Hall state at the base temperature. However, the 2/3 FQH state is usually the most robust fractional state against other competing states, whereas the 2/3 FCI state in the rhombohedral graphene/hBN system seems to lose the competition before other FCI states do. Phenomenologically, we conclude that FCI states are more robust in less disordered devices, similar to the FQH states in GaAs systems. This observation and the temperature-dependent evolution of the $\nu = 2/3$ state agree with recent theories on the competition between FCI and EQAH states.

3.2.3. Superconductivity coexisting with fractional Chern insulators. Another important observation at lower electron temperature is a superconducting state, which extends along the boundary of the insulating region near FCI states (149) (**Figure 6*a***). The superconducting transition temperature is about 60 mK. We note that chiral superconductivity has been observed in pentalayer and tetralayer rhombohedral graphene devices in the absence of moiré effects (180). At this moment, it is not clear if the superconductivity observed in moiré devices is chiral superconductivity. Coexisting superconductivity and FCI with similar charge density and displacement field conditions could enable novel gate-defined junction devices for engineering parafermions (11, 181) for topological quantum computation applications in the future.

These experiments revealed several unusual aspects that are obviously different from $MoTe_2$ and the recipe of realizing FQAHE by previous theories (182, 183). First, FQAHE was observed when the electrons in the conduction band are polarized to the opposite layer of the moiré superlattice, which imposes a very weak if not negligible moiré potential to these electrons. Second, even if a weak moiré potential is considered, one would not obtain an isolated first moiré band in the single-particle picture as in theoretical models of FCI in $tMoTe_2$. Third, the key ingredients that play an important role in FQAHE of the $tMoTe_2$, such as strong spin–orbit coupling and layer pseudospin skyrmions, are absent from the graphene/hBN moiré superlattice. Since the experiment was announced in 2023, a plethora of theoretical works have appeared to discuss these puzzles (149, 173, 174, 176–179, 184–194). New concepts such as anomalous Hall crystals were proposed (172–179), but the underlying mechanism of FQAHE and even the integer QAHE in this material system is still under debate.

3.2.4. Thermodynamic measurements. Complementary to the electron transport measurement that established FQAHE, thermodynamic measurements of the FCI gap have been performed on rhombohedral penta- and tetralayer graphene/hBN moiré superlattice devices. In a work performed on tetralayer graphene by measuring the capacitance (160), incompressible states were observed at filling factors 2/3 and 1, corresponding to the same FCI states that exhibited FQAHE in transport measurements. These states follow the Středa formula $C = \phi_0 \frac{\partial n}{\partial B}$, where C is 2/3 and 1, respectively, similar to the behavior of R_{xx} minimum under a perpendicular magnetic field in transport measurement. The gap size was extracted to be ∼24 K and 2.7 K for the integer and fractional states, respectively.

In another capacitance experiment performed on the pentalayer graphene system (107) (**Figure 6*e***), the authors focused on the situation in which electrons in the conduction band are polarized toward the moiré superlattice and subjected to a strong moiré potential. In transport measurement, no signatures of anomalous Hall were found in this situation (corresponding to the opposite displacement field from where FQAHE was observed). However, the compressibility measurement discovered integer and FCI states emerging at as low as $\sim$0.2 T (**Figure 6*f,g***). These states stem from filling factors 1, 2/3, and 1/3 and feature the corresponding Chern numbers of -1, $-2/3$, and $-1/3$, respectively. The phenomena are distinct from those observed on the weak moiré-potential side of displacement field, as the Chern numbers at the same filling factors are opposite in the strong and weak moiré potential limits. Rhombohedral graphene/hBN moiré superlattices, therefore, host FCI states in two disparate conditions that can be switched in situ by tuning the gate electric field and provide a unique testbed for any theory on achieving FCI in a general setting.

4. SUMMARY

The discovery of FQHE about forty years ago transformed our understanding of strongly interacting topological phases of matter and revealed the existence of exotic quasiparticles—anyons that could have far-reaching impact in quantum information science. The realization of the lattice analog of FQHE at zero magnetic field, i.e., FQAHE, in both $tMoTe_2$ and rhombohedral stacked multilayer graphene at elevated temperature, provides a laboratory to explore new device schemes and topological states with strong interactions. For instance, the recent discovery of valley-polarized superconductivity in rhombohedral stacked multilayer graphene (180) highlights such opportunities for creation of new strongly correlated topological states of matter not existing in other systems.

The use of moiré quantum materials offers excellent structural tunability, allowing full exploration of the many-body topological phase diagram by controlling the twist angle, moiré geometry, electric field, and doping. Rich magnetic states, topological states, and potential topological phase transitions can be explored in a controllable fashion. Those states point to new directions for both theoretical and experimental investigations. For instance, the semiconducting nature of $tMoTe_2$ offers an opportunity to harness the strong coupling among light, spin, and topology for developing topological opto-spintronics (165). The zero-field and high-temperature features of these FCI states also open up measurement opportunities that are otherwise not possible, such as photoemission spectroscopy for visualizing the Fermi sea of composite fermions.

An exciting and challenging task is to establish the anyon statistics of the zero-field FCI states and search for new states beyond those analogous to Laughlin states in the FQHE. It will be intriguing to engineer high–Chern number moiré flat bands, which could potentially host even denominate states, such as 5/2 states. Its counterpart in the FQHE is a candidate of the Moore–Read Pfaffian state. The magnetic field free and high-temperature nature of these FQAH states makes it possible to test proposals for nonabelian anyons, such as the chiral Majorana fermion. There are also theoretical proposals for engineering nonabelian anyons (such as parafermions) by interfacing superconductors with abelian FQH states. However, the strong magnetic field ($>$10 T) required for the formation of FQH states would either destroy superconductivity or generate vortices that prevent the formation of parafermions.

A platform with FQAHE would offer the opportunity to overcome the above challenges and offer a paradigm shift in researching nonabelian anyons. For instance, the coexistence of superconductivity and FCIs in rhombohedral multilayer graphene could enable the creation of atomic seamless Josephson junctions in single materials. It may eventually allow testing of the braiding statistics of nonabelian anyons in natural materials. Nonabelian anyons have a degenerate ground-state manifold. Adiabatically interchanging the position of quasiparticles causes the degenerate ground state to undergo a nontrivial unitary transformation. Such unitary operations are only determined by the topology of the interchange and may be used to construct a universal set of quantum gates. This topologically protected architecture is insensitive to local perturbations and noise, which would solve the primary roadblock—errors and quantum decoherence—to achieving the grand goal of scalable and useful quantum computation.

DISCLOSURE STATEMENT

The authors are not aware of any affiliations, memberships, funding, or financial holdings that might be perceived as affecting the objectivity of this review.

ACKNOWLEDGMENTS

D.X. and X.X. acknowledge the support from the US Department of Energy (DOE), Basic Energy Sciences (BES), under award DE-SC0012509, and Center on Programmable Quantum Materials, an Energy Frontier Research Center funded by DOE BES under award DE-SC0019443. X.X. also acknowledges the Vannevar Bush Faculty Fellowship (award number N000142512047) and Air Force Office of Scientific Research (AFOSR) FA9550-21-1-0177. T.C. acknowledges support by the US DOE, BES, under contract number DE-SC0025327. T.C. and D.X. acknowledge support by the Computational Materials Sciences Program funded by the US DOE, Office of Science, BES, Materials Sciences and Engineering Division, PNNL FWP 83557. L.J. acknowledges support from the US DOE, BES, under award DE-SC0025325, the MIT-Portugal Program Seed Fund, and NSF grant DMR-2414725. L.F. acknowledges support from the AFOSR under award number FA9550-22-1-0432 and the Simons Foundation. L.F. acknowledges the MIT SuperCloud and Lincoln Laboratory Supercomputing Center for providing computing resources.

LITERATURE CITED

1. Klitzing Kv, Dorda G, Pepper M. 1980. *Phys. Rev. Lett.* 45(6):494–97
2. Tsui DC, Störmer HL, Gossard AC. 1982. *Phys. Rev. Lett.* 48(22):1559–62
3. Laughlin RB. 1983. *Phys. Rev. Lett.* 50(18):1395–98
4. Kitaev A. 2003. *Ann. Phys.* 303(1):2–30
5. Halperin BI. 1984. *Phys. Rev. Lett.* 52(18):1583–86
6. Arovas D, Schrieffer JR, Wilczek F. 1984. *Phys. Rev. Lett.* 53(7):722–23
7. Moore G, Read N. 1991. *Nuclear Phys. B* 360(2):362–96
8. Wen XG. 1991. *Phys. Rev. Lett.* 66(6):802–5
9. Nayak C, Simon SH, Stern A, Freedman M, Das Sarma S. 2008. *Rev. Mod. Phys.* 80(3):1083–159
10. Stern A, Lindner NH. 2013. *Science* 339(6124):1179–84
11. Lindner NH, Berg E, Refael G, Stern A. 2012. *Phys. Rev. X* 2(4):041002
12. Vaezi A, Barkeshli M. 2014. *Phys. Rev. Lett.* 113(23):236804
13. Das Sarma S, Freedman M, Nayak C. 2005. *Phys. Rev. Lett.* 94(16):166802
14. de-Picciotto R, Reznikov M, Heiblum M, Umansky V, Bunin G, Mahalu D. 1997. *Nature* 389:162–64
15. Dolev M, Heiblum M, Umansky V, Stern A, Mahalu D. 2008. *Nature* 452:829–34
16. Alicea J, Fendley P. 2016. *Annu. Rev. Condens. Matter Phys.* 7:119–39
17. Bartolomei H, Kumar M, Bisognin R, Marguerite A, Berroir JM, et al. 2020. *Science* 368(6487):173–77
18. Nakamura J, Liang S, Gardner GC, Manfra MJ. 2020. *Nat. Phys.* 16(9):931–36
19. Thouless DJ, Kohmoto M, Nightingale MP, den Nijs M. 1982. *Phys. Rev. Lett.* 49(6):405–8
20. Niu Q, Thouless DJ, Wu YS. 1985. *Phys. Rev. B* 31(6):3372–77
21. Haldane FDM. 1988. *Phys. Rev. Lett.* 61(18):2015–18

22. Kane CL, Mele EJ. 2005. *Phys. Rev. Lett.* 95(22):226801
23. König M, Wiedmann S, Brüne C, Roth A, Buhmann H, et al. 2007. *Science* 318(5851):766–70
24. Bernevig BA, Hughes TL, Zhang SC. 2006. *Science* 314(5806):1757–61
25. Fu L, Kane CL. 2007. *Phys. Rev. B* 76(4):045302
26. Yu R, Zhang W, Zhang HJ, Zhang SC, Dai X, Fang Z. 2010. *Science* 329(5987):61–64
27. Chang CZ, Zhang J, Feng X, Shen J, Zhang Z, et al. 2013. *Science* 340(6129):167–70
28. Halperin BI, Jain JK. 2020. *Fractional Quantum Hall Effects*. World Scientific
29. Kalmeyer V, Laughlin RB. 1989. *Phys. Rev. B* 39(16):11879–99
30. Kol A, Read N. 1993. *Phys. Rev. B* 48(12):8890–98
31. Hafezi M, Sørensen AS, Demler E, Lukin MD. 2007. *Phys. Rev. A* 76(2):023613
32. Sørensen AS, Demler E, Lukin MD. 2005. *Phys. Rev. Lett.* 94(8):086803
33. Palmer RN, Jaksch D. 2006. *Phys. Rev. Lett.* 96(18):180407
34. Möller G, Cooper NR. 2009. *Phys. Rev. Lett.* 103(10):105303
35. Kapit E, Mueller E. 2010. *Phys. Rev. Lett.* 105(21):215303
36. Sun K, Gu Z, Katsura H, Das Sarma S. 2011. *Phys. Rev. Lett.* 106(23):236803
37. Tang E, Mei JW, Wen XG. 2011. *Phys. Rev. Lett.* 106(23):236802
38. Neupert T, Santos L, Chamon C, Mudry C. 2011. *Phys. Rev. Lett.* 106(23):236804
39. Sheng DN, Gu Z-C, Sun K, Sheng L. 2011. *Nat. Commun.* 2:389
40. Regnault N, Bernevig BA. 2011. *Phys. Rev. X* 1(2):021014
41. Xiao D, Zhu W, Ran Y, Nagaosa N, Okamoto S. 2011. *Nat. Commun.* 2:596
42. Dean CR, Wang L, Maher P, Forsythe C, Ghahari F, et al. 2013. *Nature* 497:598–602
43. Ponomarenko LA, Gorbachev RV, Yu GL, Elias DC, Jalil R, et al. 2013. *Nature* 497:594–97
44. Hunt B, Sanchez-Yamagishi JD, Young AF, Yankowitz M, LeRoy BJ, et al. 2013. *Science* 340(6139):1427–30
45. Li G, Luican A, Lopes dos Santos JMB, Castro Neto AH, Reina A, et al. 2010. *Nat. Phys.* 6(6):109–13
46. Bistritzer R, MacDonald AH. 2011. *PNAS* 108(30):12233–37
47. Cao Y, Fatemi V, Demir A, Fang S, Tomarken SL, et al. 2018. *Nature* 556:80–84
48. Cao Y, Fatemi V, Fang S, Watanabe K, Taniguchi T, et al. 2018. *Nature* 556:43–50
49. Sharpe AL, Fox EJ, Barnard AW, Finney J, Watanabe K, et al. 2019. *Science* 365(6453):605–8
50. Serlin M, Tschirhart CL, Polshyn H, Zhang Y, Zhu J, et al. 2020. *Science* 367(6480):900–3
51. Spanton EM, Zibrov AA, Zhou H, Taniguchi T, Watanabe K, et al. 2018. *Science* 360(6384):62–66
52. Xie Y, Pierce AT, Park JM, Parker DE, Khalaf E, et al. 2021. *Nature* 600:439–43
53. Park H, Cai J, Anderson E, Zhang Y, Zhu J, et al. 2023. *Nature* 622:74–79
54. Lu Z, Han T, Yao Y, Reddy AP, Yang J, et al. 2024. *Nature* 626(8000):759–64
55. Wu F, Lovorn T, Tutuc E, Martin I, MacDonald AH. 2019. *Phys. Rev. Lett.* 122(8):086402
56. Yu H, Chen M, Yao W. 2019. *Natl. Sci. Rev.* 7(1):12–20
57. Zhai D, Yao W. 2020. *Phys. Rev. Mater.* 4(9):094002
58. Liu K, Zhang L, Cao T, Jin C, Qiu D, et al. 2014. *Nat. Commun.* 5(1):4966
59. He J, Hummer K, Franchini C. 2014. *Phys. Rev. B* 89(7):075409
60. Mak KF, Shan J. 2022. *Nat. Nanotechnol.* 17(7):686–95
61. Huang D, Choi J, Shih CK, Li X. 2022. *Nat. Nanotechnol.* 17(3):227–38
62. Xiao D, Liu GB, Feng W, Xu X, Yao W. 2012. *Phys. Rev. Lett.* 108(19):196802
63. Cao T, Wang G, Han W, Ye H, Zhu C, et al. 2012. *Nat. Commun.* 3(1):887
64. Zhang X, Wang C, Liu X, Fan Y, Cao T, Xiao X. 2024. *Nat. Commun.* 15:4223
65. Wang C, Zhang XW, Liu X, He Y, Xu X, et al. 2024. *Phys. Rev. Lett.* 132(3):036501
66. Devakul T, Crépel V, Zhang Y, Fu L. 2021. *Nat. Commun.* 12:6730
67. Li H, Kumar U, Sun K, Lin SZ. 2021. *Phys. Rev. Res.* 3(3):L032070
68. Crépel V, Fu L. 2023. *Phys. Rev. B* 107(20):L201109
69. Wu M, Li J. 2021. *PNAS* 118(50):e2115703118
70. Yasuda K, Wang X, Watanabe K, Taniguchi T, Jarillo-Herrero P. 2021. *Science* 372(6549):1458–62
71. Enaldiev VV, Zólyomi V, Yelgel C, Magorrian SJ, Fal'ko VI. 2020. *Phys. Rev. Lett.* 124(20):206101
72. Magorrian SJ, Enaldiev VV, Zólyomi V, Ferreira F, Fal'ko VI, Ruiz-Tijerina DA. 2021. *Phys. Rev. B* 104(12):125440

73. Cai J, Anderson E, Wang C, Zhang X, Liu X, et al. 2023. *Nature* 622:63–68
74. Zeng Y, Xia Z, Kang K, Zhu J, Knüppel P, et al. 2023. *Nature* 622:69–73
75. Foutty BA, Kometter CR, Devakul T, Reddy AP, Watanabe K, et al. 2024. *Science* 384(6693):343–47
76. Jia Y, Yu J, Liu J, Herzog-Arbeitman J, Qi Z, et al. 2024. *Phys. Rev. B* 109(20):205121
77. Mao N, Xu C, Li J, Bao T, Liu P, et al. 2024. *Commun. Phys.* 7(1):262
78. Reddy AP, Alsallom F, Zhang Y, Devakul T, Fu L. 2023. *Phys. Rev. B* 108(8):085117
79. Qiu WX, Li B, Luo XJ, Wu F. 2023. *Phys. Rev. X* 13(4):041026
80. Yu J, Herzog-Arbeitman J, Wang M, Vafek O, Bernevig BA, Regnault N. 2024. *Phys. Rev. B* 109(4):045147
81. Reddy AP, Fu L. 2023. *Phys. Rev. B* 108(24):245159
82. Abouelkomsan A, Reddy AP, Fu L, Bergholtz EJ. 2024. *Phys. Rev. B* 109(12):L121107
83. Morales-Durán N, Wei N, Shi J, MacDonald AH. 2024. *Phys. Rev. Lett.* 132(9):096602
84. Lu T, Santos LH. 2024. *Phys. Rev. Lett.* 133(18):186602
85. Dong J, Wang J, Ledwith PJ, Vishwanath A, Parker DE. 2023. *Phys. Rev. Lett.* 131(13):136502
86. Goldman H, Reddy AP, Paul N, Fu L. 2023. *Phys. Rev. Lett.* 131(13):136501
87. Stern A, Fu L. 2024. *Phys. Rev. Lett.* 133(24):246602
88. Reddy AP, Paul N, Abouelkomsan A, Fu L. 2024. *Phys. Rev. Lett.* 133(16):166503
89. Wang C, Zhang XW, Liu X, Wang J, Cao T, Xiao D. 2025. *Phys. Rev. Lett.* 134(7):076503
90. Xu C, Mao N, Zeng T, Zhang Y. 2025. *Phys. Rev. Lett.* 134(6):066601
91. Ahn CE, Lee W, Yananose K, Kim Y, Cho GY. 2024. *Phys. Rev. B* 110(16):L161109
92. Chen F, Luo WW, Zhu W, Sheng DN. 2025. *Nat. Commun.* 16:2115
93. Anderson E, Fan FR, Cai J, Holtzmann W, Taniguchi T, et al. 2023. *Science* 381(6655):325–30
94. Park H, Cai J, Anderson E, Zhang X, Liu X, et al. 2025. *Nat. Phys.* 21:549–55
95. Xu X. 2024. *Progress in fractional quantum anomalous Hall effects*. Talk presented at Moiré Materials: A New Paradigm in Tunable Quantum Matter, KITP, UCSB, Aug. 20. **https://online.kitp.ucsb.edu/online/moire-c24/xu/**
96. Kang K, Qiu Y, Shen B, Lee K, Xia Z, et al. 2025. Preprint, arXiv:2501.02525v3 [cond-mat.mes-hall]
97. Lezama IG, Arora A, Ubaldini A, Barreteau C, Giannini E, et al. 2015. *Nano Lett.* 15:2336–42
98. Robert C, Picard R, Lagarde D, Wang G, Echeverry JP, et al. 2016. *Phys. Rev. B* 94(15):155425
99. Wang L, Shih EM, Ghiotto A, Xian L, Rhodes DA, et al. 2020. *Nature* 19:861–66
100. Ghiotto A, Shih EM, Pereira GSSG, Rhodes DA, Kim B, et al. 2021. *Nature* 597:345–49
101. Park H, Li W, Hu C, Beach C, Gonçalves M, et al. 2025. Preprint, arXiv:2503.10989v1 [cond-mat.mes-hall]
102. Ji Z, Park H, Barber ME, Hu C, Watanabe K, et al. 2024. *Nature* 635:578–83
103. Redekop E, Zhang C, Park H, Cai J, Anderson E, et al. 2024. *Nature* 635:584–89
104. Anderson E, Cai J, Reddy AP, Park H, Holtzmann W, et al. 2024. *Nature* 635:590–95
105. Xu F, Sun Z, Jia T, Liu C, Xu C, et al. 2023. *Phys. Rev. X* 13(3):031037
106. Xu F, Sun Z, Li J, Zheng C, Xu C, et al. 2025. Preprint, arXiv:2504.06972v1 [cond-mat.mes-hall]
107. Aronson SH, Han T, Lu Z, Yao Y, Butler JP, et al. 2025. *Phys. Rev. X* 15:031026
108. Willett R, Eisenstein JP, Störmer HL, Tsui DC, Gossard AC, English JH. 1987. *Phys. Rev. Lett.* 59(15):1776–79
109. Jain JK. 1989. *Phys. Rev. Lett.* 63(2):199–202
110. Halperin BI, Lee PA, Read N. 1993. *Phys. Rev. B* 47(12):7312–43
111. Willett RL, Ruel RR, West KW, Pfeiffer LN. 1993. *Phys. Rev. Lett.* 71(23):3846–49
112. Kang W, Störmer HL, Pfeiffer LN, Baldwin KW, West KW. 1993. *Phys. Rev. Lett.* 71(23):3850–53
113. Goldman VJ, Su B, Jain JK. 1994. *Phys. Rev. Lett.* 72(13):2065–68
114. Eisenstein JP, Pfeiffer LN, West KW. 1992. *Phys. Rev. Lett.* 69(26):3804–7
115. Read N. 2001. *Phys. B Condens. Matter* 298(1):121–28
116. Read N, Green D. 2000. *Phys. Rev. B* 61(15):10267–97
117. Morf RH. 1998. *Phys. Rev. Lett.* 80(7):1505–8
118. Banerjee M, Heiblum M, Umansky V, Feldman DE, Oreg Y, Stern A. 2018. *Nature* 559:205–10
119. Zhang YH. 2024. *Phys. Rev. B* 110(15):155102
120. Xu F, Chang X, Xiao J, Zhang Y, Liu F, Sun Z, et al. 2025. *Nat. Phys.* 21:542–48

121. Kang K, Shen B, Qiu Y, Zeng Y, Xia Z, et al. 2024. *Nature* 628:522–26
122. Sodemann Villadiego I. 2024. *Phys. Rev. B* 110(4):045114
123. Shi Y, Kahn J, Niu B, Fei Z, Sun B, et al. 2019. *Sci. Adv.* 5(2):eaat8799
124. Lipson HS, Stokes AR. 1942. *Proc. R. Soc. Lond. Ser. A* 181(984):101–5
125. Wilhelm H, Croset B, Medjahdi G. 2007. *Carbon* 45(12):2356–64
126. Lui CH, Li Z, Chen Z, Klimov PV, Brus LE, Heinz TF. 2011. *Nano Lett.* 11(1):164–69
127. Min H, MacDonald AH. 2008. *Prog. Theor. Phys. Suppl.* 176:227–52
128. Zhang F, Sahu B, Min H, MacDonald AH. 2010. *Phys. Rev. B* 82(3):035409
129. Koshino M, McCann E. 2009. *Phys. Rev. B* 80(16):165409
130. Zhang F, Jung J, Fiete GA, Niu Q, MacDonald AH. 2011. *Phys. Rev. Lett.* 106(15):156801
131. Lui CH, Li Z, Mak KF, Cappelluti E, Heinz TF. 2011. *Nat. Phys.* 7(12):944–47
132. Bao W, Jing L, Velasco J Jr., Lee Y, Liu G, et al. 2011. *Nat. Phys.* 7(12):948–52
133. Zhang L, Zhang Y, Camacho J, Khodas M, Zaliznyak I. 2011. *Nat. Phys.* 7(12):953–57
134. Zou K, Zhang F, Clapp C, MacDonald A, Zhu J. 2013. *Nano Lett.* 13(2):369–73
135. Heeger AJ, Kivelson S, Schrieffer JR, Su WP. 1988. *Rev. Mod. Phys.* 60(3):781–850
136. Velasco J Jr., Jing L, Bao W, Lee Y, Kratz P, et al. 2012. *Nat. Nanotechnol.* 7(3):156–60
137. Lee Y, Tran D, Myhro K, Velasco J, Gillgren N, et al. 2014. *Nat. Commun.* 5(1):5656
138. Myhro K, Che S, Shi Y, Lee Y, Thilahar K, et al. 2018. *2D Mater.* 5(4):045013
139. Weitz RT, Allen MT, Feldman BE, Martin J, Yacoby A. 2010. *Science* 330(6005):812–16
140. Geisenhof FR, Winterer F, Seiler AM, Lenz J, Xu T, et al. 2021. *Nature* 598(7879):53–58
141. Han T, Lu Z, Scuri G, Sung J, Wang J, et al. 2024. *Nat. Nanotechnol.* 19(2):181–87
142. Liu K, Zheng J, Sha Y, Lyu B, Li F, et al. 2024. *Nat. Nanotechnol.* 19(2):188–95
143. Shi Y, Xu S, Yang Y, Slizovskiy S, Morozov SV, et al. 2020. *Nature* 584(7820):210–14
144. Zhang Y, Tang TT, Girit C, Hao Z, Martin MC, et al. 2009. *Nature* 459(7248):820–23
145. Ju L, Shi Z, Nair N, Lv Y, Jin C, et al. 2015. *Nature* 520(7549):650–55
146. Ju L, Wang L, Cao T, Taniguchi T, Watanabe K, et al. 2017. *Science* 358(6365):907–10
147. Yang J, Chen G, Han T, Zhang Q, Zhang YH, et al. 2022. *Science* 375(6586):1295–99
148. Han T, Lu Z, Yao Y, Yang J, Seo J, et al. 2024. *Science* 384(6696):647–51
149. Lu Z, Han T, Yao Y, Hadjri Z, Yang J, et al. 2025. *Nature* 637:1090–95
150. Xiao D, Yao W, Niu Q. 2007. *Phys. Rev. Lett.* 99(23):236809
151. Han T, Lu Z, Scuri G, Sung J, Wang J, et al. 2023. *Nature* 623(7985):41–47
152. Zhou H, Xie T, Ghazaryan A, Holder T, Ehrets JR, et al. 2021. *Nature* 598(7881):429–33
153. Xue J, Sanchez-Yamagishi J, Bulmash D, Jacquod P, Deshpande A, et al. 2011. *Nat. Mater.* 10(4):282–85
154. Decker R, Wang Y, Brar VW, Regan W, Tsai HZ, et al. 2011. *Nano Lett.* 11(6):2291–95
155. Yankowitz M, Xue J, Cormode D, Sanchez-Yamagishi JD, Watanabe K, et al. 2012. *Nat. Phys.* 8(5):382–86
156. Chen G, Jiang L, Wu S, Lyu B, Li H, et al. 2019. *Nat. Phys.* 15(3):237–41
157. Zhang YH, Mao D, Cao Y, Jarillo-Herrero P, Senthil T. 2019. *Phys. Rev. B* 99(7):075127
158. Chen G, Sharpe AL, Fox EJ, Zhang YH, Wang S, et al. 2020. *Nature* 579(7797):56–61
159. Sha Y, Zheng J, Liu K, Du H, Watanabe K, et al. 2024. *Science* 384(6694):414–19
160. Choi Y, Choi Y, Valentini M, Patterson CL, Holleis LFW, et al. 2025. *Nature* 639(8054):342–47
161. Deng Y, Yu Y, Shi MZ, Guo Z, Xu Z, et al. 2020. *Science* 367(6480):895–900
162. Li T, Jiang S, Shen B, Zhang Y, Li L, et al. 2021. *Nature* 600(7890):641–46
163. Park Y, Kim Y, Chittari BL, Jung J. 2023. *Phys. Rev. B* 108(15):155406
164. Xie J, Huo Z, Lu X, Feng Z, Zhang Z, et al. 2025. *Nat. Mater.* 24:1042–48
165. Anderson E, Park H, Yang K, Cai J, Tanaguchi T, et al. 2025. *Phys. Rev. X* 15:031057
166. Xia J, Pan W, Vicente C, Adams E, Sullivan N, et al. 2004. *Phys. Rev. Lett.* 93(17):176809
167. Liu Y, Pappas C, Shayegan M, Pfeiffer L, West K, Baldwin K. 2012. *Phys. Rev. Lett.* 109(3):036801
168. Eisenstein J, Cooper K, Pfeiffer L, West K. 2002. *Phys. Rev. Lett.* 88(7):076801
169. Deng N, Kumar A, Manfra MJ, Pfeiffer L, West K, Csathy GA. 2012. *Phys. Rev. Lett.* 108(8):086803
170. Chen S, Ribeiro-Palau R, Yang K, Watanabe K, Taniguchi T, et al. 2019. *Phys. Rev. Lett.* 122(2):026802
171. Kumar A, Csáthy G, Manfra M, Pfeiffer L, West K. 2010. *Phys. Rev. Lett.* 105(24):246808
172. Seiler AM, Geisenhof FR, Winterer F, Watanabe K, Taniguchi T, et al. 2022. *Nature* 608(7922):298–302

173. Dong J, Wang T, Wang T, Soejima T, Zaletel MP, et al. 2024. *Phys. Rev. Lett.* 133(20):206503
174. Zhou B, Yang H, Zhang YH. 2024. *Phys. Rev. Lett.* 133(20):206504
175. Zeng Y, Guerci D, Crépel V, Millis AJ, Cano J. 2024. *Phys. Rev. Lett.* 132(23):236601
176. Soejima T, Dong J, Wang T, Wang T, Zaletel MP, et al. 2024. *Phys. Rev. B* 110(20):205124
177. Dong Z, Patri AS, Senthil T. 2024. *Phys. Rev. B* 110(20):205130
178. Tan T, Devakul T. 2024. *Phys. Rev. X* 14(4):041040
179. Sheng D, Reddy AP, Abouelkomsan A, Bergholtz EJ, Fu L. 2024. *Phys. Rev. Lett.* 133(6):066601
180. Han T, Lu Z, Hadjri Z, Shi L, Wu Z, et al. 2025. *Nature* 643:654–61
181. Clarke DJ, Alicea J, Shtengel K. 2013. *Nat. Commun.* 4(1):1348
182. Vishwanath A. 2023. Zero field fractional Hall states, now in graphene heterostructures. Journal Club for Condensed Matter Physics. **https://doi.org/10.36471/JCCM_December_2023_03**
183. Parameswaran S. 2024. Anomalous Hall Crystals or Moire Chern Insulators? Spontaneous versus explicit translational symmetry breaking in graphene pentalayers. Journal Club for Condensed Matter Physics. **https://doi.org/10.36471/JCCM_January_2024_02**
184. Kwan YH, Yu J, Herzog-Arbeitman J, Efetov DK, Regnault N, Bernevig BA. 2025. *Phys. Rev. B* 112:075109
185. Yu J, Herzog-Arbeitman J, Kwan YH, Regnault N, Bernevig BA. 2025. *Phys. Rev. B* 112:075110
186. Guo Z, Lu X, Xie B, Liu J. 2024. *Phys. Rev. B* 110(7):075109
187. Kudo K, Nakai R, Nomura K. 2024. *Phys. Rev. B* 110(24):245135
188. Xie M, Das Sarma S. 2024. *Phys. Rev. B* 109(24):L241115
189. Dong Z, Patri AS, Senthil T. 2024. *Phys. Rev. Lett.* 133(20):206502
190. Huang K, Li X, Das Sarma S, Zhang F. 2024. *Phys. Rev. B* 110(11):115146
191. Huang K, Das Sarma S, Li X. 2025. *Phys. Rev. B* 111(7):075130
192. Tan T, May-Mann J, Devakul T. 2024. Preprint, arXiv:2409.06775v1 [cond-mat.mes-hall]
193. Das Sarma S, Xie M. 2024. *Phys. Rev. B* 110(15):155148
194. Wei Z, Wu A-K, Gonçalves M, Lin S-Z. 2025. *Phys. Rev. B* 111(3):035116